Monthly Notices
of the
ROYAL ASTRONOMICAL SOCIETY

Mon. Not. R. Astron. Soc. **400,** 1121–1131 (2009) doi:10.1111/j.1365-2966.2009.15617.x

A spatially resolved map of the kinematics, star formation and stellar mass assembly in a star-forming galaxy at $z = 4.9$

A. M. Swinbank,[1⋆] T. M. Webb,[2] J. Richard,[1] R. G. Bower,[1] R. S. Ellis,[3] G. Illingworth,[4] T. Jones,[3] M. Kriek,[5] I. Smail,[1] D. P. Stark[6] and P. van Dokkum[7]

[1] *Institute for Computational Cosmology, Durham University, South Road, Durham DH1 3LE*
[2] *Department of Physics, McGill University, 3600 rue University, Montreal, QC H2A 2T8, Canada*
[3] *Astronomy Department, California Institute of Technology, 105-24, Pasadena, CA 91125, USA*
[4] *UCO/Lick Observatory, University of California, Santa Cruz, CA 95064, USA*
[5] *Department of Astrophysical Sciences, Princeton University, Princeton, NJ 08544, USA*
[6] *Institute of Astronomy, University of Cambridge, Madingley Road, Cambridge CB3 0HA*
[7] *Department of Astronomy, Yale University, New Haven, CT 06520, USA*

Accepted 2009 August 26. Received 2009 August 24; in original form 2009 May 22

ABSTRACT

We present a detailed study of the spatially resolved kinematics, star formation and stellar mass in a highly amplified galaxy at $z = 4.92$ behind the lensing cluster MS 1358+62. We use the observed optical, near- and mid-infrared imaging from *Hubble Space Telescope* ACS & NICMOS and *Spitzer* IRAC to derive the stellar mass and the Gemini/NIFS IFU to investigate the velocity structure of the galaxy from the nebular [O II]λλ3726.8,3728.9 emission. Using a detailed gravitational lens model, we account for lensing amplification factor 12.5 ± 2.0 and find that this intrinsically L^* galaxy has a stellar mass of $M_\star = 7 \pm 2 \times 10^8\,\mathrm{M}_\odot$, a dynamical mass of $M_{\rm dyn} = 3 \pm 1 \times 10^9 csc^2(i)\,\mathrm{M}_\odot$ (within of 2 kpc) and a star formation rate of $42 \pm 8\,\mathrm{M}_\odot\,\mathrm{yr}^{-1}$. The source-plane UV/optical morphology of this galaxy is dominated by five discrete star-forming regions. Exploiting the dynamical information we derive masses for individual star-forming regions of $M_{\rm cl} \sim 10^{8-9}\,\mathrm{M}_\odot$ with sizes of ∼200 pc. We find that, at a fixed size, the star formation rate density within these H II regions is approximately two orders of magnitude greater than those observed in local spiral/starburst galaxies, but consistent with the most massive H II regions in the local Universe such as 30 Doradus. Finally, we compare the spatially resolved nebular emission-line velocity with the Lyα and UV interstellar medium (ISM) lines and find that this galaxy is surrounded by a galactic scale outflow in which the Lyα appears redshifted by $\sim$150 km s^{-1} and the UV-ISM lines blueshifted by ~ -200 km s^{-1} from the (systemic) nebular emission. The velocity structure of the outflow mirrors that of the nebular emission suggesting the outflow is young ($\lesssim$15 Myr), and has yet to burst out of the system. Taken together, these results suggest that this young galaxy is undergoing its first major epoch of mass assembly.

Key words: galaxies: evolution – galaxies: formation – galaxies: high-redshift – galaxies: individual: MS 1358+62arc.

1 INTRODUCTION

Deep imaging surveys, particularly with *Hubble Space Telescope* (*HST*), have now uncovered thousands of star-forming galaxies in the redshift range $z = 4$–6 (e.g. Ouchi et al. 2004; Giavalisco et al. 2004; Yoshida et al. 2006; Beckwith et al. 2006; Bouwens et al. 2007). Studying such galaxies are key steps towards understanding the physical processes that drive galaxy formation in the early Universe, probing the properties of galaxies when they formed their first generation of stars. Concentrated follow-up of Lyman-break galaxies at this epoch has provided estimates of stellar masses ($\sim 10^{9-10}\,\mathrm{M}_\odot$), ages (∼150–300 Myr) and hence inferred star formation rates of a few tens $\mathrm{M}_\odot\,\mathrm{yr}^{-1}$ (Verma et al. 2007; McLure et al. 2009; Stark et al. 2009). With high specific star formation rates, these young galaxies are likely assembling their first significant stellar mass. Moreover, since this epoch is within ∼300 Myr of the end of reionization (assuming reionization was completed by $z \sim 6$) many of these galaxies should have been actively star forming at $z \gtrsim 7$. As such, probing the ubiquity of star-forming

⋆E-mail: a.m.swinbank@dur.ac.uk

galaxies, the ionizing photon density from star formation and their relation to AGN are important issues, potentially allowing us to understand how and when the first galaxies were assembled and how the Universe was reionized. Moreover, theoretical models suggest that the most rapid epoch of dark halo assembly for galaxies such as the Milky Way occurs at $z \sim 5$ (Mo & White 2002; Okamoto et al. 2005). Through detailed studies of the physical properties of galaxies at this epoch (such as masses and star formation rates), we can accurately assess their contribution to the mass growth of galaxies like the Milky Way, and their effect on the gaseous intergalactic medium (IGM).

Indeed, one of the key findings in recent years is the discovery that a significant fraction of high-redshift galaxies are surrounded by 'superwinds' (e.g. Franx et al. 1997; Pettini et al. 2002b; Shapley et al. 2003; Bower et al. 2004; Wilman et al. 2005; Swinbank et al. 2007) – starburst and/or active galactic nuclei (AGN)-driven outflows which expel gas from the galaxy potential and hence play no further role in the star formation history of the galaxy. Such feedback processes may offer natural explanations to the shape and normalization of the local luminosity function (Benson et al. 2003; Bower et al. 2006; Croton et al. 2006) and offer natural explanations as to why only 10 per cent of the baryons cool to form stars (White & Rees 1978; Balogh et al. 2001). Although velocity offsets between star-forming regions and outflowing gas of several hundred km s^{-1} have been measured (suggestive of large-scale outflows), constraining the geometry and mass loading is vital to test whether the outflows are truly large scale [as often observed in low-redshift Ultra-Luminous Infrared Galaxies (ULIRGS); Martin 2005], or whether the outflows are confined to individual star-forming regions. Such constraints are vital in order to test whether the outflowing material escapes into the IGM, or whether it eventually stalls, fragments and drains back down on to the galaxy disc, causing further bursts of star formation.

However, probing the masses, star formation rates and interaction between star formation and gas dynamics which is routine at $z \sim 2$ (e.g. Genzel et al. 2006; Förster Schreiber et al. 2006; Swinbank et al. 2006b; Law et al. 2007; Stark et al. 2008; Lehnert et al. 2009; Law et al. 2009) is difficult beyond $z \sim 3$ due to a combination of surface brightness dimming and the smaller physical sizes of the earliest systems (and the strong evolution in the UV luminosity function between $z \sim 3$ and 6 means there are fewer luminous sources; e.g. Stark et al. 2009). Prior to the launch of *James Webb Space Telescope (JWST)*, one particularly appealing route to study the internal structures of primitive galaxies at $z \sim 5$ is to target galaxies which have been highly magnified by their serendipitous alignment with a foreground massive cluster. The lensing magnification (up to a factor of 30× in the most extreme cases) has two effects: the galaxy image is amplified at a fixed surface brightness so that the galaxy image appears both brighter and larger. By combining gravitational lensing with resolved spectroscopic imaging, detailed maps of the sizes, dynamics and hence masses of both young galaxies and even starburst/H II regions within these galaxies can be made. Such observations can be used to investigate whether the physical conditions for star formation were significantly different from comparably luminous galaxies at $z \sim 2$ and galaxies today. Indeed, gravitational lensing and resolved spectroscopic imaging have been used to investigate galaxy dynamics on ∼1 kpc scales from $z = 1$ to 3 (e.g. Swinbank et al. 2003, 2006a; Nesvadba et al. 2006; Salucci et al. 2007), whilst coupling lensing with adaptive optics (AO) source-plane studies can even reach $\lesssim$100 pc (Stark et al. 2008; Jones et al., in preparation).

Studying the physical processes of galaxy formation on scales comparable to the largest H II regions is likely to have broad implications for our understanding of the dominant mechanism by which galaxies at high redshift assemble their stellar mass, and what processes drive the star formation activity (Bournaud & Elmegreen 2009). For example, recent hydro-dynamical simulations have suggested that continuous gas accretion (so-called 'cold-flows') may play an important role in driving star formation at $z > 2$ (Davé 2008; Dekel et al. 2009). In such models, these cold streams keep the rotating disc configuration intact, but with turbulent star-forming clumps which eventually merge to form a central spheroid. This is a provocative result, as it has generally been accepted that major mergers are the dominant mechanism by which massive galaxies assemble their stellar mass (Conselice, Rajgor & Myers 2008). However, to test such models in detail, the galaxy velocity field and the turbulent speeds on scales comparable to individual H II regions in a large sample of high-redshift, star-forming galaxies are required. Resolved dynamics of galaxies at $z \sim 2$ have lent support to the cold-stream model, but at the spatial scales available in non-lensed galaxies (1–4 kpc) it is difficult to draw definitive conclusions. Nevertheless, the advances in instrumentation (particularly sensitive integral-field units and AO) are beginning to allow studies of the kinematics, distribution of star formation, gas and stars and chemical properties in high-redshift star-forming galaxies which can be fed into (and thus test) numerical simulations.

In this paper, we report the detailed follow-up of a lensed galaxy at $z = 4.92$ behind the lensing cluster MS 1358+62, first studied in detail by Franx et al. (1997). We use the *HST* ACS & NICMOS imaging to investigate the rest-frame UV/optical morphology. Together with *Spitzer* Infrared Array Camera (IRAC) imaging we construct the spectral energy distribution (SED) to estimate the stellar mass. Using the Gemini/Near-Infrared Integral Field Spectrometer (NIFS) integral field unit, we map the [O II]λλ3726.2,3728.9 emission-line strength and dynamics, distribution of star formation and outflow energetics. We have adopted a standard Λ cold dark matter cosmology with $H_0 = 72\,\mathrm{km\,s^{-1}}$, $\Omega_\mathrm{M} = 0.27$ and $\Omega_\Lambda = 0.73$. All quoted magnitudes are on the AB system.

2 OBSERVATIONS AND DATA REDUCTION

2.1 Optical-, near- and mid-infrared imaging

Details of the optical, near- and mid-infrared observations of this galaxy cluster are given in Richard et al. (2008). Briefly, the lensing cluster MS 1358+62 ($z_\mathrm{cl} = 0.33$; α: 13:59:50 δ: +62:31:05, J2000) was observed with *HST* Advanced Camera for Surveys (ACS) and Near Infrared Camera and Multi-Object Spectrometer (NICMOS) as part of program PID: 9717 & 10504 using the 435W, 475W, 625W, 775W, 850LP, F110W and F160W filters with integration times 5.4–16 ks each in the optical bands and ∼19 ks each in the near-infrared bands. The optical and near-infrared imaging reach typical 5σ depths of AB = 26.5–27.5 mag. We also include *K*-band photometry from Soifer et al. (1998) which reaches a 5σ sensitivity of $K_\mathrm{AB} \sim 23$. The *Spitzer* IRAC 3.6, 4.5, 5.8 and 8.0 μm imaging comprises 2.4 ks in each band, reaching 5σ depths of $AB \sim 24$ (Richard et al. 2008).

The $z = 4.92$ arc lies approximately 21 arcsec southwest of the brightest cluster galaxy at α: 13:59:48.7 δ: +62:30:48.34 (J2000) and was discovered during a spectroscopic survey of this cluster by Franx et al. (1997) in which the redshifted Lyα and UV interstellar medium (ISM) lines were used to derive an unambiguous redshift of $z = 4.92$ (a companion galaxy at the same redshift located approximately 200 kpc away in the source-plane was also discovered during the same survey). In Fig. 1, we show a true-colour *HST* ACS

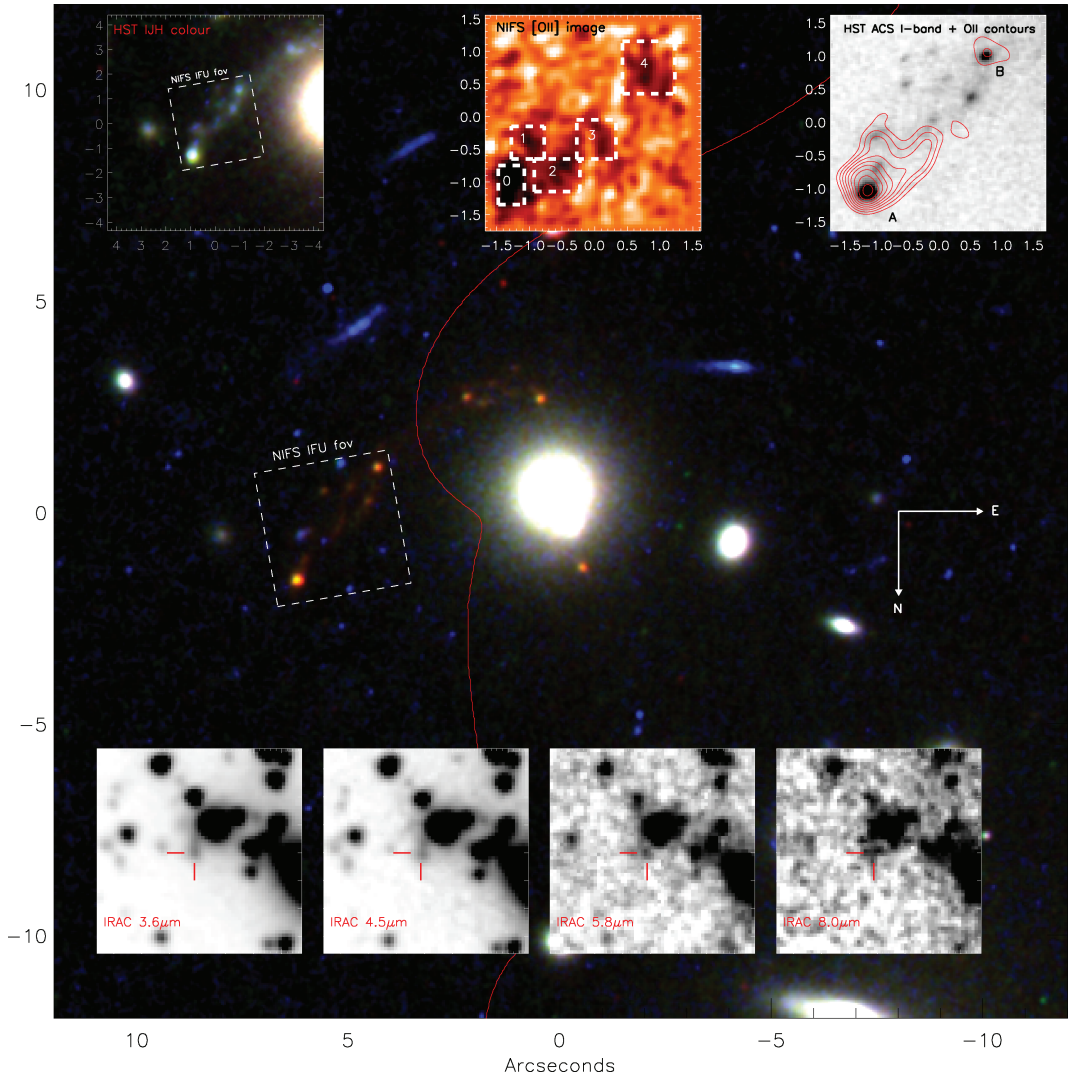

Figure 1. True-colour *HST* ACS *VRI*-band image of the lensed $z = 4.92$ galaxy behind MS 1358+62. The image is centred at the position of a bright cluster elliptical at $\alpha = 13{:}39{:}49.51$, $\delta = +62{:}30{:}48.69$ (note that the BCG lies approximately 20 arcsec south). The $z = 4.92$ critical curve from our best-fitting lens model is also overlaid. The *HST* imaging clearly shows the galaxy resolved into two images of the background galaxy, with the morphology dominated by up to six star-forming regions surrounded by a diffuse halo. The dashed white box shows the NIFS IFU field of view used to cover the $z = 4.92$ galaxy image. The upper-left insets show a colour image generated from the NICMOS F110 and F160 images showing that the *J*- and *H*-band morphologies clearly trace the observed *VRI*-band morphology. The upper-middle panel shows the white light (wavelength collapsed) image of the [O II] emission from the IFU datacube (dark grey denotes highest intensity). The boxes (labelled 0–4) denote the regions from which spectra were extracted (see Fig. 4). The upper-right insets show the *HST* ACS *I*-band image (dark grey denotes high intensity) with contours from the [O II] emission-line image overlaid, showing that the [O II] emission-line morphology follows that seen in the rest-frame UV. The contours denote [O II] emission-line flux levels of 0.2–1 $\times$ 10^{-16} erg s^{-1} cm^{-2} arcsec^{-2} in increasing in units of 0.1 $\times$ 10^{-16} erg s^{-1} cm^{-2} arcsec^{-2}. The lower four insets show the *Spitzer* IRAC 3.6, 4.5, 5.8 and 8.0 μm images around the lensed galaxy. In each panel, we mark the position of the brightest component of the $z = 4.92$ arc, which is clearly visible in all four channels (each of these panels is 30 arcsec on a side).

VIz-band image of the cluster core around the $z = 4.92$ arc. We also show an ACS/NICMOS *IJH*-band true-colour image, as well as thumb-nails around the galaxy in the four IRAC images showing that the galaxy is detected from *V* band to the IRAC 8.0 μm channel.

To calculate the photometry of the lensed galaxy, we first consider the bright elliptical galaxy located ∼6 arcsec due east (which has a low surface brightness halo which extends beyond the $z = 4.92$ galaxy image). We construct a model of the elliptical galaxy surface photometry using the IRAF BMODEL ellipse fitting algorithm (Jedrzejewski, Davies & Illingworth 1987) (we note that we mask the $z = 4.92$ galaxy image during the fit). In this model, the surface photometry includes the c_4 Fourier coefficient (which is necessary to describe the boxiness of the isophotes), but all other Fourier terms were forced to zero. We then subtract the best-fitting model from the galaxy image and then use SEXTRACTOR (Bertin & Arnouts 1996) to estimate the residual background within the frame. Since accurate colours are required to derive the SED we calculate the magnitude of the lensed galaxy in the various passbands using an elliptical aperture (approximately 3 $\times$ 1.5 arcsec^2 centred on the first image of the arc as covered by the NIFS IFU). This aperture is constructed from the co-added *I*- and *z*-band images since these represent the highest signal-to-noise ratio in the $z = 4.92$ arc. The same aperture is then applied to all of the images to measure the photometry. In the IRAC channels, we apply an aperture correction to account for the

Table 1. Observed aperture photometry for MS 1358+62arc.

Filter	mag (AB)
B_{475}	>26.5
V_{625}	23.50 ± 0.08
I_{775}	22.05 ± 0.05
z_{850}	22.12 ± 0.05
J_{110}	22.18 ± 0.08
H_{160}	22.38 ± 0.08
K	22.52 ± 0.20
3.6 μm	22.90 ± 0.10
4.5 μm	23.14 ± 0.10
5.8 μm	23.43 ± 0.25
8.0 μm	23.50 ± 0.25

Note. To convert to intrinsic magnitudes (corrected for the lensing amplification factor $12.5 \pm 2.0\times$) add 2.7 mag.

flux lying outside the aperture (∼0.6–0.8 mag from 3.6 to 8.0 μm) as determined from bright (unsaturated) point sources in the image.

In Table 1, we give the observed photometry of the galaxy from the *HST* ACS & NICMOS and *Spitzer* IRAC imaging, and in Fig. 3 we show the observed photometry with the best-fitting model SED overlaid (see Section 3.2). We note that the large error bars (particularly at 5.8 and 8.0 μm) reflect the uncertainty in recovering the photometry from the arc after modelling and removing the foreground elliptical galaxy which dominates the light, particularly at the reddest wavelengths. We also note that there is MIPS 24 μm coverage of this cluster with a bright source at the position of the galaxy. However, due to the blending with the foreground lensing galaxy (located ∼6 arcsec east), it is not possible to reliably deblend the photometry from the elliptical galaxy.

2.2 Spectroscopic imaging

Three-dimensional spectroscopic imaging observations around the redshifted [O II]λλ3726.2,3728.9 Å emission line were taken with the Gemini-North NIFS between 2006 February 08 and 2006 February 09 during science verification time.[1]

The Gemini-NIFS IFU uses an image slicer to take a 3.0 × 3.0 arcsec^2 field and divides it into 29 slices of width 0.103 arcsec. The dispersed spectra from the slices are reformatted on the detector to provide two-dimensional spectro-imaging, in our case using the K-band grism covering a wavelength range of 2.00–2.43 μm. The observations were undertaken using an ABC sequence in which we chopped to 6 arcsec to blank sky to achieve sky subtraction. Individual exposures were 600 s and each observing block was 3.6 ks, which was repeated four times for resulting in an integration time of 14.4 ks (with a total of 9.6 ks on source and 4.8 ks on sky).

We reduced the data with the standard Gemini IRAF NIFS pipeline which includes extraction, sky-subtraction, wavelength calibration and flat-fielding. Residual OH sky emission lines were removed using the sky-subtraction techniques described in Davies (2007). To accurately align and mosaic the individual datacubes we created white light (wavelength collapsed) images around the redshifted [O II] line from each observing block and centroid the galaxy within the data cube. These were then spatially aligned and co-added using an average with a 3σ clipping threshold to remove remaining cosmetic defects and cosmic rays. Flux calibration was carried out by observing a bright A0V standard star (HIP 78017) at similar airmass to the target galaxy immediately after each observing block. From the reduced standard star cube, we measure a K-band seeing of full width at half-maximum (FWHM) = 0.45 arcsec. We note that accounting for lensing amplification factor $12.5 \pm 2.0\times$ (derived in Section 3) this corresponds to a source-plane FWHM of ∼0.6 kpc. The spectral resolution of the data (measured from the sky-lines at ∼2.2 μm) is $R = \lambda/\Delta\lambda = 5300$ which corresponds to $\sigma = 3$ Å or 25 km s^{-1}. In all following sections, quoted linewidths are deconvolved for the instrumental resolution.

3 ANALYSIS

3.1 Lens modelling

We first estimate the amplification of the galaxy by making use of the updated gravitational lens model from Richard et al. (2008). Fig. 1 shows the cluster region around the lensed galaxy with the best fit $z = 4.92$ critical curve overlaid. Using the mapping between image and source-plane co-ordinates, we ray-trace the $z = 4.92$ galaxy image and reconstruct the source-plane morphology, deriving a luminosity-weighted magnification factor $\mu = 12.5 \pm 2.0\times$ (which corresponds to $\Delta m = 2.7 \pm 0.2$ mag). The error bar on μ is derived by ray-tracing the family of acceptable gravitational lens models which adequately reproduce the multiply imaged galaxies in the cluster.

Accounting for lensing amplification, the intrinsic magnitude of the galaxy is $I_{\rm AB} = 24.94 \pm 0.08$. For comparison, deep imaging surveys of Lyman-break galaxies at $z \sim 5$ have derived an L^* of $i_{\rm AB} \sim 25.3$ suggesting that the $z = 4.92$ galaxy studied here is typical of the UV-continuum selected samples at this redshift (e.g. Ouchi et al. 2004).

In Fig. 2, we show the reconstructed source-plane image of the galaxy which shows that the rest-frame UV/optical morphology is elongated, but is dominated by two star-forming regions separated by ∼4 kpc with at least four more lower-surface brightness regions within the galaxy and surrounded by a low surface brightness halo.

To estimate the size of the source-plane PSF in each band, we first measure the size of the PSF using the $R \sim 19$ star located 5 arcsec due south of the arc, which has an FWHM = 0.10, 0.33, 0.30 arcsec in the observed I, J and H bands, respectively. The two largest star-forming regions (at approximately [1.8,2.0] and [−1.0,−2.1] kpc in Fig. 2) have an I band FWHM which is marginally resolved (FWHM = 0.17 ± 0.03 arcsec), but both are unresolved in J and H bands. Since the lensing amplification of the source has a preferential direction, we reconstruct the source-plane image of the star at the locations of the brightest star-forming regions and find that the ACS PSF transforms to 0.06 × 0.014 arcsec^2 (320 × 85 pc). Both of the brightest two H II regions are marginally resolved in the I-band imaging (FWHM = 0.17 ± 0.03 arcsec and FWHM = 0.15 ± 0.04 for regions A and B in Fig. 1, respectively) corresponding to FWHM = 500 ± 100 pc and FWHM = 400 ± 150 pc (deconvolved for PSF). We note that the size of the largest of these two H II regions is comparable to the size measured by Franx et al. (1997)

[1] Programme ID: GN-2006-SV-130. Based on observations obtained at the Gemini Observatory, which is operated by the Association of Universities for Research in Astronomy, Inc., under a cooperative agreement with the NSF on behalf of the Gemini partnership: the National Science Foundation (United States), the Particle Physics and Astronomy Research Council (United Kingdom), the National Research Council (Canada), CONICYT (Chile), the Australian Research Council (Australia), CNPq (Brazil) and CONICET (Argentina).

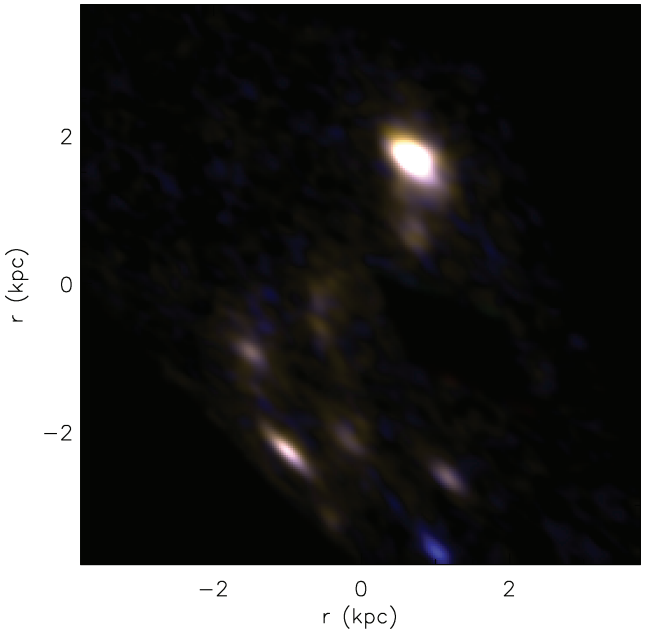

Figure 2. True-colour *HST* ACS *VRI*-band reconstruction of the lensed galaxy using the mass model described in Section 3. The amplification of the galaxy is a factor of 12.5 ± 2.0×. In the source-plane, the galaxy has a spatial extent of ∼4 kpc and comprises at least five discrete star-forming clumps. The largest of these is only marginally resolved, with a rest-frame optical half-light radii of ∼200 pc.

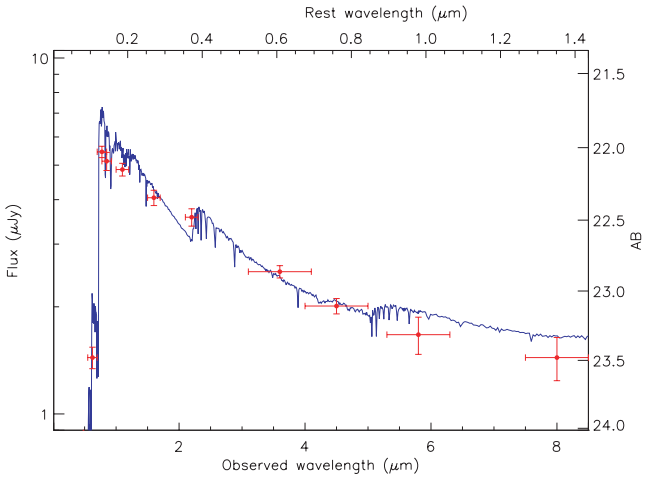

Figure 3. Observed SED of the galaxy from the observed *HST* ACS/NICMOS and *Spitzer* IRAC photometry. We overlay the best-fitting SED from HYPERZ which predicts a young age of ∼20 Myr and moderate ($A_v = 0.25$) reddening. Fitting the observed photometry we derive a stellar mass (correct for lensing amplification) of $M_\star = 7 \pm 2 \times 10^8\,M_\odot$.

(FWHM ∼ 390 pc) from *HST* WFPC2 observations. In the *J* and *H* bands, the source-plane PSFs are approximately 800 × 220 pc and 300 × 1 kpc in the NIFS [O II] emission-line map. We therefore conservatively suggest sizes of FWHM $\lesssim$ 500 and 400 pc in *J* and *H* bands, respectively, and $\lesssim$600 pc in the O II emission-line map for the two H II regions, *A* and *B*, respectively. We discuss the implications of these sizes in Section 3.6, but note that clearly higher spatial resolution IFU observations using laser-guide star AO would be very valuable to further constrain their sizes.

3.2 Stellar mass

Soifer et al. (1998) use optical and near-infrared photometry to estimate the stellar mass in this galaxy, deriving $M_\star = 2$–$16 \times 10^9\,M_\odot$. Here, we make use of the much deeper ACS/NICMOS and, particularly, IRAC imaging in order to improve the estimate of the stellar mass. We infer the stellar mass of the galaxy by fitting the latest Charlot & Bruzual stellar population synthesis models (Bruzual & Charlot 2003) to the observed SED [which include an improved treatment of the thermally pulsating asymptotic giant branch (TP-AGB) phase of stellar evolution]. Following Stark et al. (2009), we allow 200 age steps from 10^5 to 10^9 yr (approximately logarithmically spaced), with a Salpeter (1955) initial mass function (IMF) and consider both a solar and sub-solar ($0.2\,Z_\odot$) metallicity. We fit both constant star formation histories and exponentially decaying (τ) models with e-folding decay times of 100 Myr. We consider the effects of dust in the modelling by adopting the Calzetti, Kinney & Storchi-Bergmann (1994) reddening law [using colour excesses of $E(B-V) = 0.0$, 0.03, 0.05, 0.1, 0.3 and 1.0]. The resulting template SEDs are convolved with the filter response curves, and by comparing the observed magnitudes and their associated errors, we compute a reduced χ^2 value for each set of parameters [age, $E(B-V)$ and normalization]. The 1σ uncertainties are calculated from the parameter range which produce $\Delta\chi^2 = 1$ with respect to the best-fitting SED (whilst marginalizing over the other free parameters).

For consistency, we first model the *IJHK*-band galaxy photometry from Soifer et al. (1998), deriving acceptable solutions with $E(B-V) = 0.06$–0.4, ages $= 1 \times 10^{6-9}$ Myr and stellar masses of $M_\star = 1 \times 10^9$–$4 \times 10^{10}\,M_\odot$ (which is consistent with Soifer et al. 1998). However, the much deeper *HST* ACS/NICMOS and *Spitzer* photometry (*VIzJHK* and IRAC 3.6,4.5,5.8,8.0 μm) allow much better constraints to be derived, and we infer a best-fitting SED with an age of 14 ± 7 Myr, an $E(B-V) = 0.05 \pm 0.05$ and a stellar mass of $M_\star = 7 \pm 2 \times 10^8\,M_\odot$, with a $0.2\,Z_\odot$ metallicity template marginally preferred over solar metallicity (although formally the difference in $\Delta\chi^2$ is less than 1σ between the two). We note that the constant star formation and τ models provide equally good fits to the data, with stellar masses which vary by <5 per cent. We also attempt fits excluding the IRAC 5.8 and 8.0 μm photometry, but the resulting stellar mass and age agree within the 1σ errors. We note that the stellar mass derived here is significantly lower (at least a factor of >3×) than that derived by Soifer et al. (1998), which most likely arises due to the improved photometric constraints and very young age as suggested by the IRAC photometry.

3.3 Star formation rate and dynamics

Next, we use the spatially resolved [O II]λλ3726.8,3728.9 emission-line maps from our NIFS IFU observation to estimate the distribution of star formation and dynamics within the galaxy. As Fig. 1 shows, the nebular line emission is clearly patchy, and dominated by the brightest regions seen in the *HST* ACS and NICMOS imaging. Collapsing the brightest regions within the galaxy we find that the integrated [O II] emission-line flux is $f_{[\mathrm{O\,II}]} = 1.5 \pm 0.3 \times 10^{-16}$ erg cm^{-2} s^{-1}. Accounting for an amplification factor ($\mu = 12.5 \pm 2.0\times$) and using the conversion between [O II] emission-line flux and star formation rate from Kennicutt (1998) we derive an intrinsic star formation rate of $\mathrm{SFR}_{[\mathrm{O\,II}]} = 42 \pm 8\,M_\odot\,\mathrm{yr}^{-1}$ (uncorrected for reddening). This star formation rate is consistent with the 3σ upper-limit of SFR ∼ $80\,M_\odot\,\mathrm{yr}^{-1}$ (corrected for lensing) from SCUBA 850 μm imaging (Knudsen, van der Werf & Kneib

2008). We note that if the star formation rate derived from the [O II] emission-line flux (SFR $= 42 \pm 8\,M_\odot\,yr^{-1}$) has been sustained, then it takes just ∼15 Myr to build a stellar mass of $M_\star = 7 \times 10^8\,M_\odot$, suggesting the current burst may be the first major episode of star formation within this galaxy (which is also consistent with the young SED). It is also useful to note that the starburst intensity (SFR/area) for the galaxy ($S_e \sim 4 \times 10^{11}\,L_\odot\,kpc^{-2}$) is comparable with local (e.g. Meurer et al. 1997) and high-redshift (e.g. Giavalisco, Steidel & Macchetto 1996; Steidel et al. 1996) galaxies, suggesting the same mechanisms may limit the starburst intensity at $z \sim 5$ as those at lower redshifts.

We also use the spatially resolved [O II] emission-line doublet from the NIFS IFU observations to investigate the dynamics of the galaxy. By collapsing the velocity field from the brightest regions within the data cube we derive a peak-to-peak velocity gradient of $\Delta v = 180 \pm 20\,km\,s^{-1}$ across 4 kpc in projection (Fig. 5). If these dynamics reflect virialized motion within a bound system, we estimate a dynamical mass of $M_{dyn}(<2\,kpc) = 3 \pm 1 \times 10^9 csc^2(i)\,M_\odot$. Adopting a canonical inclination of 30° suggests a dynamical mass of $M_{dyn} \sim 10^{10}\,M_\odot$. Alternatively, the dynamical mass can also be estimated via the velocity dispersion using the relation $M_{dyn} = C\sigma^2 r/G$. The factor C depends on the galaxy mass distribution and velocity field, and ranges from $C \lesssim 1$ to $C \gtrsim 5$ [depending on the mass density profile, velocity anisotropy and relative contribution to σ from random motion, rotation and assumption of spherical or disc-like system; see Erb et al. (2006) for a detailed discussion]. Adopting $C = 3.4$ (such that a direct comparison to star-forming galaxies at $z = 2$–3 can be made; Erb et al. 2006), we derive a dynamical mass of $M_{dyn} \sim 10^{10}\,M_\odot$. This dynamical mass is approximately six to 10 times smaller than the median Lyman-break galaxy mass at $z \sim 3$ for which masses have been measured using similar techniques (e.g. Erb et al. 2006; Förster Schreiber et al. 2006; Law et al. 2009), but comparable to that of the only other star-forming galaxy at these redshifts with measured nebular emission-line dynamics (RCS0224-002 arc at $z = 4.88$; Swinbank et al. 2007). We also note that the inferred dynamical mass is much larger than the stellar mass. If the central regions are baryon dominated, this may suggest that the gas reservoir makes up >75–90 per cent of the baryons. Clearly, observations of the cold molecular gas [such as the redshifted CO(1–0) or CO(3–2)] would be required to test this.

Next, we investigate the properties of individual star-forming regions within the galaxy. In Fig. 4, we show the extracted spectra from the strongest line emitting regions from the galaxy. The two largest star-forming regions in Fig. 1 have velocity dispersions of $\sigma_0 = 86 \pm 15$ and $\sigma_4 = 80 \pm 15\,km\,s^{-1}$. Taken with their sizes derived above we derive masses of star-forming regions of the order of 6–9 $\times 10^8\,M_\odot$ (we note that in calculating these masses, we have used the same value of C as above for simplicity), and star formation rates of $SFR_0 = 12 \pm 1$ and $SFR_4 = 6 \pm 1\,M_\odot\,yr^{-1}$, respectively, suggesting that up to half of the total star formation is occurring within two dense regions and outside the nuclear regions.

3.4 Comparison with rest-frame UV

Franx et al. (1997) discuss the morphology and rest-frame UV spectral properties of this galaxy in detail. In particular, the UV-ISM absorption lines show velocity variations of the order of 200 km s^{-1} along the arc with the Si IIλ1260 line systematically blueshifted with respect to the Lyα emission, and an asymmetric Lyα emission line with a red tail. As discussed by Franx et al. (1997), these spectral features are naturally explained by an outflow model, in which the

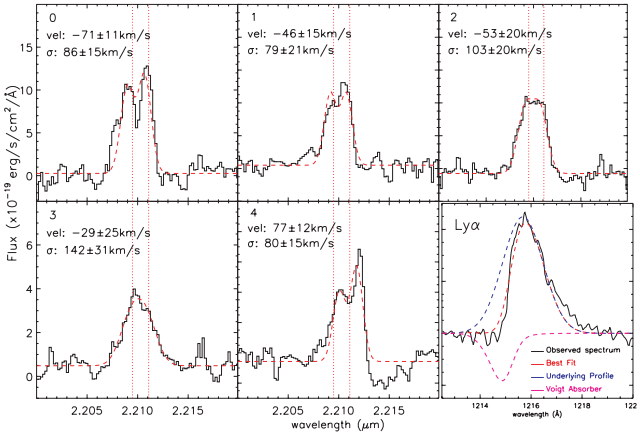

Figure 4. One-dimensional spectrum of the five star-forming regions within the $z = 4.92$ galaxy from the NIFS IFU observations. In all panels, we show the position of the [O II]$\lambda\lambda$3726.8,3728.9 doublet at a fixed redshift of $z = 4.9296$. In each panel, we also overlay the best-fitting spectrum and give the (rest-frame) velocity offset from the systemic redshift and linewidth of the best-fitting double Gaussian profile. From the spectra, the velocity gradient of $\Delta v = 180 \pm 20\,km\,s^{-1}$ can easily be seen. The final panel shows the one-dimensional spectrum of the $z = 4.92$ galaxy around the Lyα emission line (from Franx et al. 1997), showing the asymmetric line profile. Using the systemic redshift measured from the nebular emission, we de-redshifted the spectrum and find that the asymmetric emission line is best fit with an underlying Gaussian emission-line profile (blue dashed line) combined with a Voigt absorber in the blue wing.

blue side of the Lyα line has been absorbed by outflowing neutral H I. The description of the line profile is very typical of the emission profiles seen in other Lyman-break galaxies. Indeed, velocity offsets between the nebular emission lines (such as Hα) and UV-ISM emission/absorption lines (such as Lyα and Si IIλ1260) are now common in high-redshift star-forming galaxies, and are usually interpreted as evidence for large-scale starburst-driven outflow (Teplitz et al. 2000; Pettini et al. 2002b; Erb et al. 2003). Such a model provides a good description of the integrated properties of high-redshift galaxies and more detailed observations of local starbursts (e.g. Tenorio-Tagle et al. 1999; Heckman et al. 2000; Pettini et al. 2002b; Shapley et al. 2003; Grimes et al. 2006). In this model, the Lyα emission comes from photons emitted from the star-forming regions. To reach the observer these must pass through part of the foreground (blueshifted) shell. This absorption causes the peak emission wavelength to appear redshifted relative to the nebular emission lines. In addition, photons may be scattered or emitted from the receding shell. Photons that are either created on the inner surface of the shell (e.g. by UV irradiation from the starburst) or multiply scattered within the receding shell will acquire the mean velocity of the outflow and will be seen as redshifted by the observer (see the discussion of Hansen & Oh 2006).

With the systemic velocity of the galaxy measured from the [O II] emission, we can compare the nebular emission-line velocity gradient seen in this galaxy with those observed in Lyα emission and UV-ISM lines, as well as crudely estimating the energetics of the outflow. Using the systemic redshift measured from the [O II] emission-line doublet ($z = 4.9296 \pm 0.0002$), the Lyα appears systematically redshifted from the systemic redshift by 100–200 km s^{-1} across the 4 kpc extent of the galaxy (Fig. 5). Moreover, the UV-ISM absorption lines are also correspondingly blueshifted by ∼200 ± 100 km s^{-1}. This is typical of high-redshift, star-forming galaxies. However, strikingly, the velocity gradient in the nebular emission

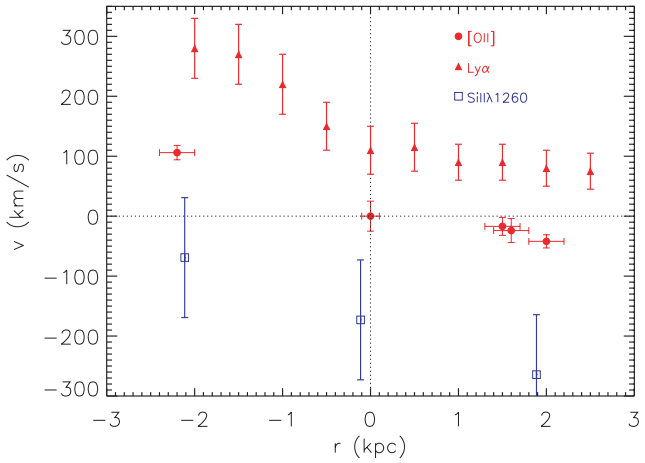

Figure 5. Extracted, one-dimensional velocity gradient along the long axis of the galaxy (source-plane). The velocity gradient of ∼180 km s^{-1} observed in the [O II] emission is mirrored by the Lyα and UV-ISM lines, although they appear systematically offset from the systemic by 150–200 km s^{-1}, suggesting that the galaxy is surrounded by a young galactic scale outflow which has yet to decouple and burst out of the galaxy. Using the velocity offsets and spatial extent of the galaxy, we suggest the outflow is $\lesssim$15 Myr old.

is mirrored in both the Lyα and UV-ISM lines. The fact that the velocity structure of the outflow follows that seen in the nebular emission suggests the outflow has yet to decouple from the galaxy. Indeed, assuming that the outflow is no larger than the spatial extent of the stellar component of the galaxy ($\lesssim$2 kpc), then for a constant velocity of 150 km s^{-1} it takes just 15 Myr to travel 2 kpc. This suggests that the young outflows from individual H II regions have not yet merged to form a superwind surrounding the galaxy.

To test whether a young outflow is energetically feasibly, first we de-redshift the rest-frame UV spectrum using the systemic redshift. In Fig. 4, we show the region around the Lyα emission in the rest frame, clearly showing the asymmetric profile. A single Gaussian profile fit suggests a velocity offset from the systemic redshift of ∼200 km s^{-1}. However, a much better fit ($\Delta\chi^2 > 25$) is obtained by modelling the emission line with an underlying Gaussian profile (fixed in wavelength at 1215.67 Å) with a Voigt profile absorber in the blue wing. In this fit, the emission-line width and intensity of the underlying Gaussian profile are allowed to vary, as are the velocity, impact parameter (b) and column density (n) of the Voigt profile. The best-fitting model has a Voigt profile centred -300 ± 100 km s^{-1} from the systemic with $b \sim 70$ km s^{-1} and $n \sim 4 \times 10^{17}$ cm^{-2}. Allowing the centroid of the underlying Gaussian emission-line profile to vary, the column density increases to $n \sim 3 \times 10^{18}$ cm^{-2} and $b \sim 120$ km s^{-1} with an underlying Gaussian profile with centroid $\Delta v = -100 \pm 30$ km s^{-1} from that predicted from the [O II] emission (we note that the improvement in χ^2 between the two fits is $\Delta\chi^2 < 4$ and so indistinguishable, although fixing the underlying Gaussian profile at the systemic redshift is more physical). We caution that both of these column densities are near the flat part of the curve of growth causing degeneracies between $N_{\rm H}$ and b and so come with considerable uncertainty. However, we can at least test whether such a value is reasonable using the UV absorption lines and assuming an ionization state for the ISM. Using the rest-frame UV spectroscopy we measure (rest-frame) equivalent widths of W_o(Si IIλ1260.4) = 0.30 ± 0.07 Å, W_o(O Iλ1302.1) = 1.69 ± 0.07 Å, W_o(CIIλ1334.5) = 0.32 ± 0.07 Å, W_o(Si IVλ1393.4) = 0.24 ± 0.06 Å and W_o(Si IVλ1402.8) = 0.29 ± 0.06 Å. Since we cannot constrain the ionization state or metallicity of the galaxy (we only have one transition from each species), we adopt a simple approach and assume that the ionization and metallicity are comparable to that of cB58 at $z = 2.72$ which has an abundance of ∼0.4 solar (Pettini et al. 2002a). Assuming $\log[X/H] = -4.86$ for Si IIλ1260.4 and an equivalent width of W_o(Si IIλ1260.4) = 0.30 ± 0.07 Å (which corresponds to a column density of $N_{\rm Si\,II} \sim 2 \times 10^{13}$ cm^{-2}) we derive a hydrogen column density of $\sim 2 \times 10^{17}$ cm^{-2}. Although we caution this estimate comes with considerable uncertainty, the column density estimated from the Lyα line profile, or crudely using the UV-ISM absorption lines, appears, at least, to be consistent within a factor of ∼4×.

Although there are uncertainties in the column density of the outflowing shell, it is interesting to consider the energetics. For a normal stellar IMF, supernovae provide $\sim 10^{49}$ erg per solar mass of stars (e.g. Benson et al. 2003), thus for a galaxy with a star formation rate of SFR = 42 ± 7 M$_\odot$ yr^{-1}, $\sim 5 \times 10^{50}$ erg are available per year. We estimate the distance of the shell from the galaxy by assuming that the linear size of the region covered by the swept up shell is no larger than the spatial extent as the galaxy (which seems reasonable given the velocity structure of the outflow appears to follow the nebular emission-line velocity). As noted, at a velocity of ∼150 km s^{-1} it takes 15 Myr to travel out to a distance of 2 kpc; within this time, supernovae will provide a total energy of $E_{\rm SNe} \sim 5 \times 10^{57}$ erg. Clearly, there are a number of uncertainties in this estimate: not least that the outflow may have decelerated from an initial higher velocity which would reduce the time-scale. Nevertheless, we can estimate the mass of the outflow via: $M_{\rm outflow} = AN_{\rm H\,I} \times m_{\rm H}/x$ where $N_{\rm H\,I}$ is the column density, A is the area of the cone and $m_{\rm H}$ is the atomic mass of hydrogen. Adopting the value of the observed column density derived above ($N_{\rm H\,I} \sim \times 10^{17-18}$ cm^{-2}) and that the outflowing material is uniform over an area of ∼10 kpc^2, the total mass of the outflow is $3 \times 10^4/x$ M$_\odot$, where x is the neutral H I fraction. The kinetic energy of the outflow is then $E_{\rm K} = \frac{1}{2}mv^2 \sim 10^{53}/x$ erg. Thus, the outflow is easily energetically feasible even if the neutral fraction is as low as 0.01 per cent. The low inferred mass loading and kinetic energy in the shell are in stark contrast to the $z = 4.88$ galaxy behind the lensing cluster RCS0224−002 in which similar observations suggest a large-scale, bi-polar outflow surrounds the galaxy (Swinbank et al. 2007). In this galaxy, the outflow has a high-mass loading (comparable or greater than the star formation rate) and appears to be located >30 kpc from the galaxy, escaping at a speed of up to 500 km s^{-1}. The strong contrast between the two galaxies so far studied at these early times therefore suggests strong diversity in the outflow energetics of young galaxies at a high redshift, clearly illustrating the need for more targets and follow-up to test the ubiquity and impact of outflows at these early times.

3.5 Comparison of age and mass estimates

It is useful to compare the various stellar and dynamical mass and age estimates, since these reflect the build up of stellar mass in this system. First, the stellar mass estimated from the rest-frame UV-near-infrared SED of the galaxy is much smaller than the dynamical mass estimated from the dynamics. Similar results have been found in the $z \sim$ 2–3 population. Erb et al. (2006) find ∼10 per cent of star-forming systems with stellar masses which are approximately 10 per cent of the dynamical mass. These systems also tend to be the youngest, <20 Myr (e.g. HDF-BX1397 is an excellent example). Thus, although the stellar mass estimate appears small compared

to the dynamical mass (possibly suggesting a large gas reservoir makes up the rest of the baryonic material), the galaxy does not appear to be at odds with comparable observations of the galaxy population at $z \sim 2$–3.

It is also interesting to note that the age estimated from the SED (∼15 Myr) is comparable to that derived from the instantaneous star formation rate (at a SFR of 42 $M_\odot$ yr^{-1} it takes just ∼17 Myr to build a stellar mass of 7×10^8 $M_\odot$). Finally, the dynamical age of the outflow (∼15 Myr) is young, and consistent with a scenario in which a starburst wind is in the process of accelerating material from the galaxy into the halo and/or IGM. Together, these mass and age estimated are all suggestive of a young galaxy experiencing its first major epoch of mass assembly.

3.6 Properties of the largest star-forming regions

Owing to the magnification of the galaxy, the source-plane resolution of the optical and near-infrared imaging we are also able to estimate the masses, sizes and luminosities of the brightest star-forming (H II) regions within the galaxy to test whether the physical conditions for star formation at $z \sim 5$ are very different to galaxies today. Using the results from Section 3.1, we estimate the brightest star-forming regions within the galaxy have diameters of the order *of* ∼300–400 pc from the *HST* and NIFS observations. Using the velocity dispersions measured from the IFU observations, this suggests dynamical masses of ∼6–9 × 10^8 $M_\odot$ each and mass densities of ∼3000 $M_\odot$ pc^{-2}. In Fig. 6, we show the correlation between size and mass of H II regions (and starburst complexes) in local galaxies. Clearly, the size density of the brightest star-forming regions in MS 1358+62 arc are consistent with the most massive clusters seen in star-forming galaxies. Next, we compare the luminosities and sizes of the brightest H II regions to those locally. In Fig. 7, we show the correlation between size and luminosity of local H II regions (Kennicutt 1988; Gonzalez Delgado & Perez 1997; Kennicutt et al. 2003; Lee et al. 2007) and show the position of the two brightest star-forming regions from MS 1358+62 arc. As Fig. 7 shows, the two brightest H II regions appear to have star formation activity which is substantially higher (at a fixed size) than those typically derived from local star-forming galaxies. However, before we interpret this offset in detail, there are two caveats which must be considered. We first note that this comparison relies on a conversion between [O II] (in the $z = 4.92$ arc) and Hα locally. However, as Kewley, Geller & Jansen (2004) point out, the conversion between the star formation rate derived from Hα and [O II] never varies by more than a factor of 2, even for extreme ranges in metallicity and reddening. Indeed, targeting the nebular emission-line ratios of ∼25 lensed galaxies, Richard et al. (in preparation) (see also Pettini et al. 2001) derive a median Hα/[O II] emission-line flux ratio of Hα/[O II] $= 2.5 \pm 0.8$ (median redshift of this sample $z = 2.4 \pm 0.4$), which is slightly larger, but consistent with the values locally (Hα/[O II] $= 1.8 \pm 0.5$; Kewley et al. 2004). Thus, it seems unlikely that there is a factor of 100× increase in the [O II]/Hα emission-line ratio between $z = 2$ and 5.

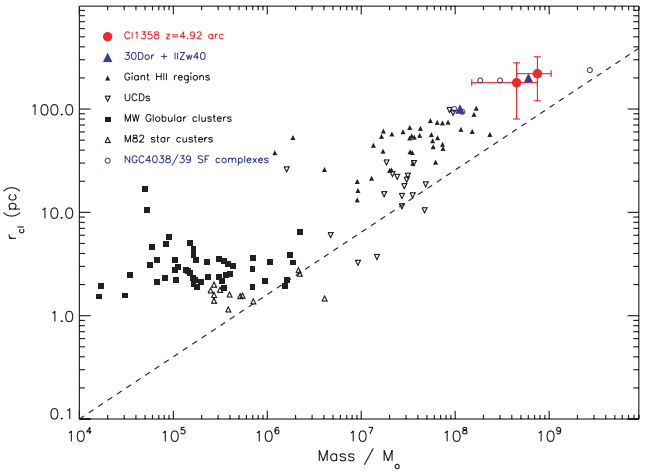

Figure 6. Mass versus size for H II regions in local galaxies compared to the two H II regions in MS 1358+62 showing that the two brightest star-forming regions are large, massive star clusters, but have comparable densities to H II regions found locally. The squares denote Milky Way globular clusters (Pryor & Meylan 1993; Harris 1996), inverted open triangles represent Ultra-Compact Dwarfs (Haşegan et al. 2005; Evstigneeva et al. 2007; Hilker et al. 2007) and open triangles are M82 superstar clusters from McCrady & Graham (2007). The solid triangles denote giant H II regions from Fuentes-Masip et al. (2000). The dashed line shows the predicted cluster radius as a function of mass (after accounting for mass loss) from Murray (2009).

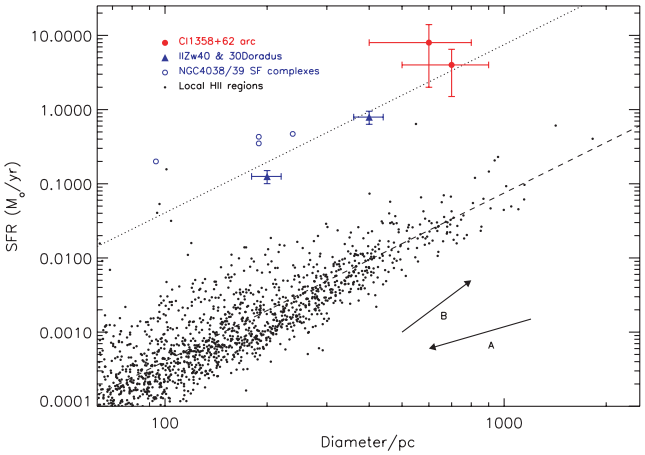

Figure 7. Correlation between size and star formation rate from Hα for H II regions in local galaxies. The solid points denote the H II regions in local star-forming galaxies from Kennicutt (1988), Kennicutt et al. (2003), Lee et al. (2007). We also show the star formation rate–size relation for 30 Doradus (the largest, local H II region in the LMC) as well as the giant starburst region in the nearby galaxy II Zw 40 (Vanzi et al. 2008) and the Antennae (Bastian et al. 2006). The dashed line shows a fit to the H II regions in nearby spiral galaxies whilst the dotted line is the same but shifted in luminosity at a fixed size by a factor of 100×. The two H II regions in MS 1358+62 arc are shown by the solid red points where the x error bars denote the range of size estimates from the source-plane IFU and ACS reconstructions, and the y error bar denotes the error in the flux measurement, lens modelling uncertainty and the range of possible [O II]/Hα emission-line flux ratios from Kewley et al. (2004) for extreme ranges in metallicity and reddening. The two H II regions in the $z = 4.92$ galaxy appear to be scaled up versions of the most luminous star-forming regions observed locally, even though they are observed when the Universe was less than 1 Gyr old.

Secondly, we caution that the isophotes used to extract H II regions' sizes and luminosities are very different at $z = 0$ compared to those at $z \sim 5$ (even accounting for lensing). Hence, to test whether we can reliably compare H II region sizes and luminosities at high-redshift to those locally, we make use of the extensive Hα narrow-band imaging of local galaxies, in particular from SINGS (Kennicutt et al. 2003) and 11 HUGS (Lee et al. 2007). Using 175 Hα narrow-band images from these samples, we test the effect of redshifting the $z = 0$ galaxy images and re-extracting the size–luminosity relation. First, we use the Hα narrow-band imaging and construct the size–luminosity relation for local galaxies using isophotes ranging

from 1×10^{-18} to 1×10^{-15} erg cm^{-2} s^{-1} arcsec^{-2}. We find that, as the isophotal flux is increased, the lower-luminosity H II regions fall below the detection threshold, whilst only the cores of the higher luminosity H II regions are identified. This results in the local relation remaining in tact, with fewer H II regions identified. In Fig. 7, we show a vector (labelled 'A') which shows the typical direction H II regions follow as the extraction isophote is increased.

Next, we test the effect of artificially redshifting the imaging from a spatial resolution of ∼10 pc (0.5 arcsec at 5 Mpc) to a resolution of ∼200 pc and extract the H II regions at a fixed isophote. This binning has the effect of merging H II regions, increasing both the size and luminosity, and in Fig. 7 we show vector 'B' which denotes the track which H II regions follow as the resolution is decreased.

The simulations show that essentially the size–luminosity relation does not systematically shift as the images are redshifted, and we therefore feel confident that any offset we measure in the size–luminosity relation likely reflects a real difference in their properties (see also Melnick, Terlevich & Terlevich 2000). We note that it is entirely possible that the star-forming regions in the $z = 5$ galaxy represent an amalgamation of multiple H II regions. However, these simple simulations suggest that they will remain overluminous at a fixed size.

Next, we examine the implication of identifying H II regions at $z = 4.92$ which are significantly more luminous than those found locally. At a fixed size of 400 pc, local H II regions have star formation rates of the order of SFR $= 0.1$ M$_\odot$ yr^{-1}, thus the star-forming regions observed in the $z = 4.92$ galaxy appear to be substantially more luminous than those in local galaxies. However, at a fixed size, offsets of (up to) two orders of magnitude in luminosities are observed in the most luminous nearby H II regions and starburst galaxies (e.g. Wilson & Matthews 1995; English & Freeman 2003; Bastian et al. 2006; Vanzi et al. 2008). For example, 30 Doradus has a star formation rate of ∼0.15 M$_\odot$ yr^{-1} and a size of ∼200 pc whilst the giant H II region in the starburst galaxy II Zw 40 has a star formation rate of ∼1 M$_\odot$ yr^{-1} within 400 pc (e.g. Wilson & Matthews 1995; English & Freeman 2003; Vanzi et al. 2008), although both of these systems are of low metallicity. However, observations of massive star-clusters in NGC 4038/39 (the Antennae) also indicate young (∼5 Myr) clusters with star formation rates much higher than expected for typical star-forming galaxies (Bastian et al. 2006). Thus, the H II regions within this $z = 4.92$ galaxy appear to be scaled up versions of the most extreme H II regions observed in the local Universe. It is unclear whether this is due to the starburst mode, or low metallicity, although it is interesting to note that the most recent models of galaxy formation suggest that star formation at a high redshift may be driven by strongly unstable and fragmenting discs (e.g. Dekel et al. 2009) resulting in localized starbursts. Thus, the intense star formation observed in this galaxy will significantly affect the surrounding ISM both in distributing metals and in adding turbulence.

4 DISCUSSION AND CONCLUSIONS

After correcting for lensing magnification factor $12.5 \pm 2.0\times$, the rest-frame UV/optical morphology appears extended over ∼4 kpc, but is dominated by approximately five star-forming regions. In the source-plane the galaxy has an I-band magnitude consistent with L^* LBGs at $z \sim 5$, and an intrinsic star formation rate of SFR$_{[\rm O\,II]} = 42 \pm 8$ M$_\odot$ yr^{-1}. Using rest-frame UV-to-H-band SED we derive stellar mass of $M_\star = (7 \pm 2) \times 10^8$ M$_\odot$, which is consistent with estimates of the stellar masses of LBGs at this epoch (Verma et al. 2007; McLure et al. 2009; Stark et al. 2009). The SED is also consistent with being dominated by a young stellar population of age of 14 ± 7 Myr. Indeed, with a star formation rate of ∼42 M$_\odot$ yr^{-1}, it takes just ∼17 Myr to build this stellar mass. Together, this suggests that this galaxy is in the first major epoch of mass assembly.

The source-plane morphology is clumpy with at least five star-forming regions, separated by up to 4 kpc in projection. The brightest regions are not centrally concentrated, and the galaxy shows no signs of a central component. Using the spatially resolved spectroscopy around the [O II] emission, we derive a velocity gradient of $\Delta v = 180 \pm 20$ km s^{-1} across 4 kpc in projection, suggesting a dynamical mass of $M_{\rm dyn} = 3 \pm 1 \times 10^9\,{\rm M}_\odot csc^2(i)\,{\rm M}_\odot$. We also derive a specific star formation rate (SFR/M$_\star$) of SSFR $= 2.4 \pm 0.5 \times 10^{-8}$ yr^{-1}, consistent with the most actively star-forming, low-mass galaxies at these early times (Feulner et al. 2005).

Using the source-plane images and [O II] emission-line maps, we measure sizes and masses for the two brightest star-forming regions, deriving masses of $M_{\rm cl} = 6$–9×10^8 M$_\odot$ and individual star formation rates of SFR$_{[\rm O\,II]} \sim 10$ M$_\odot$ yr^{-1}. A comparison to local H II regions/populations shows that these are comparably massive and dense as those found in local star-forming galaxies. However, the implied star formation rate individually for these H II regions is $\gtrsim$100 times brighter than found at a fixed size. Such high star formation rates (at a fixed size) have been observed locally: e.g. 30 Doradus and II Zw 40 both have star formation rates which are >100 times larger than expected given their sizes. Thus, the H II regions within this $z = 4.92$ galaxy appear to be scaled up versions of the most extreme regions observed in the local Universe, yet observed when the Universe was $\lesssim$1 Gyr old. Could the increased luminosity within H II regions reflect real difference in the mode of star formation within massive star-forming complexes? Murray (2009) suggests that young, massive (>10^7 M$_\odot$) star-forming clusters are optically thick to far-infrared radiation resulting in high gas temperatures, and hence in higher Jeans masses. Indeed, for a star cluster with mass >10^8 M$_\odot$ (as observed in this $z = 4.92$ galaxy), the predicted Jeans mass is ∼12 M$_\odot$. This 'top-heavy' IMF has the effect of increasing the fraction of OB stars per H II region and hence increases the light-to-mass ratio (see the discussion in Murray 2009). However, since no compelling evidence for evolution in the IMF has yet been found at either low or high redshift, we view this scenario as suggestive, at best. Nevertheless, clearly spatially resolved spectroscopy of the nebular emission lines on scales comparable to H II regions would provide crucial diagnostics of the physics of star formation in the young Universe. Indeed, this intense star formation will significantly affect the surrounding ISM both in distributing metals and in adding turbulence. As such, the mechanical energy input might explain the higher turbulent speeds (hence large v/σ values) observed in primitive discs (e.g. Genzel et al. 2008; Stark et al. 2008; Law et al. 2009; Forster Schreiber et al. 2009; Lehnert et al. 2009).

Finally, we compare the nebular emission-line dynamics with spatially resolved Lyα and rest-frame UV-ISM lines and find that this galaxy is surrounded by a galactic scale outflow. The velocity gradient observed in the nebular emission is mirrored (but systematically offset) in the Lyα emission and UV-ISM absorption across ∼4 kpc, suggesting that the outflow is young (<15 Myr) and has yet to decouple from the star-forming regions and escape from the galaxy disc. Although crude, the estimated mass loading in the outflow is very small, and the kinetic energy provided by SNe from the observed star formation rate is easily enough to drive the wind.

Overall, these observations provide unique insights into the distribution of star formation, dynamics, interaction between star formation and outflow energetics and even properties of the largest

H II regions within a young galaxy seen less than 1 Gyr after the big bang on scales of just ∼200 pc. The combination of the large number of high-redshift gravitationally lensed galaxies identified by *HST* and AO assisted integral field spectrographs on 8- and 10-m telescopes should finally begin to make such critical observational studies common-place, testing the route by why early systems assemble their stellar mass, their mode of star formation and how they ultimately develop into galaxies like the Milky Way.

ACKNOWLEDGMENTS

We gratefully acknowledge an anonymous referee for a very constructive report which significantly improved the content and clarity of this paper. We also gratefully acknowledge the Gemini staff for granting SV time for these observations. We would like to thank Janice Lee for very useful discussions and for allowing us to use the 11 HUGS narrow-band imaging prior to the publication and Marijn Franx for useful discussions and providing us with the rest-frame UV spectroscopy. AMS gratefully acknowledges a Sir Norman Lockyer Royal Astronomical Society Fellowship and a Royal Society travel grant and DPS acknowledges an STFC fellowship.

REFERENCES

Balogh M. L., Pearce F. R., Bower R. G., Kay S. T., 2001, MNRAS, 326, 1228
Bastian N., Emsellem E., Kissler-Patig M., Maraston C., 2006, A&A, 445, 471
Beckwith S. V. W. et al., 2006, AJ, 132, 1729
Benson A. J., Bower R. G., Frenk C. S., Lacey C. G., Baugh C. M., Cole S., 2003, ApJ, 599, 38
Bertin E., Arnouts S., 1996, A&AS, 117, 393
Bournaud F., Elmegreen B. G., 2009, ApJ, 694, L158
Bouwens R. J., Illingworth G. D., Franx M., Ford H., 2007, ApJ, 670, 928
Bower R. G. et al., 2004, MNRAS, 351, 63
Bower R. G., Benson A. J., Malbon R., Helly J. C., Frenk C. S., Baugh C. M., Cole S., Lacey C. G., 2006, MNRAS, 370, 645
Bruzual G., Charlot S., 2003, MNRAS, 344, 1000
Calzetti D., Kinney A. L., Storchi-Bergmann T., 1994, ApJ, 429, 582
Conselice C. J., Rajgor S., Myers R., 2008, MNRAS, 386, 909
Croton D. J. et al., 2006, MNRAS, 365, 11
Davé R., 2008, MNRAS, 385, 147
Davies R. I., 2007, MNRAS, 375, 1099
Dekel A. et al., 2009, Nat, 457, 451
English J., Freeman K. C., 2003, AJ, 125, 1124
Erb D. K., Shapley A. E., Steidel C. C., Pettini M., Adelberger K. L., Hunt M. P., Moorwood A. F. M., Cuby J., 2003, ApJ, 591, 101
Erb D. K., Steidel C. C., Shapley A. E., Pettini M., Reddy N. A., Adelberger K. L., 2006, ApJ, 646, 107
Evstigneeva E. A., Gregg M. D., Drinkwater M. J., Hilker M., 2007, AJ, 133, 1722
Feulner G., Gabasch A., Salvato M., Drory N., Hopp U., Bender R., 2005, ApJ, 633, L9
Förster Schreiber N. M. et al., 2006, ApJ, 645, 1062
Forster Schreiber N. M., Genzel R., Bouche N., Cresci G., Davies R., Buschkamp P., Shapiro K., Tacconi L. J., 2009, preprint (arXiv e-prints)
Franx M., Illingworth G. D., Kelson D. D., van Dokkum P. G., Tran K., 1997, ApJ, 486, L75
Fuentes-Masip O., Muñoz-Tuñón C., Castañeda H. O., Tenorio-Tagle G., 2000, AJ, 120, 752
Genzel R. et al., 2006, Nat, 442, 786
Genzel R. et al., 2008, ApJ, 687, 59
Giavalisco M., Steidel C. C., Macchetto F. D., 1996, ApJ, 470, 189
Giavalisco M. et al., 2004, ApJ, 600, L93
Gonzalez Delgado R. M., Perez E., 1997, ApJS, 108, 199
Grimes J. P., Heckman T., Hoopes C., Strickland D., Aloisi A., Meurer G., Ptak A., 2006, ApJ, 648, 310
Hansen M., Oh S. P., 2006, MNRAS, 367, 979
Harris W. E., 1996, AJ, 112, 1487
Haşegan M. et al., 2005, ApJ, 627, 203
Heckman T. M., Lehnert M. D., Strickland D. K., Armus L., 2000, ApJS, 129, 493
Hilker M., Baumgardt H., Infante L., Drinkwater M., Evstigneeva E., Gregg M., 2007, A&A, 463, 119
Jedrzejewski R. I., Davies R. L., Illingworth G. D., 1987, AJ, 94, 1508
Kennicutt R. C., Jr, 1988, ApJ, 334, 144
Kennicutt R. C., 1998, ARA&A, 36, 189
Kennicutt R. C. Jr et al., 2003, PASP, 115, 928
Kewley L. J., Geller M. J., Jansen R. A., 2004, AJ, 127, 2002
Knudsen K. K., van der Werf P. P., Kneib J.-P., 2008, MNRAS, 384, 1611
Law D. R., Steidel C. C., Erb D. K., Larkin J. E., Pettini M., Shapley A. E., Wright S. A., 2007, ApJ, 669, 929
Law D. R., Steidel C. C., Erb D. K., Larkin J. E., Pettini M., Shapley A. E., Wright S. A., 2009, ApJ, 697, 2057
Lee J. C., Kennicutt R. C., Funes, José G. S. J., Sakai S., Akiyama S., 2007, ApJ, 671, L113
Lehnert M. D., Nesvadba N. P. H., Tiran L. L., Matteo P. D., van Driel W., Douglas L. S., Chemin L., Bournaud F., 2009, ApJ, 699, 1660
Martin C. L., 2005, ApJ, 621, 227
McCrady N., Graham J. R., 2007, ApJ, 663, 844
McLure R. J., Cirasuolo M., Dunlop J. S., Foucaud S., Almaini O., 2009, MNRAS, 395, 2196
Melnick J., Terlevich R., Terlevich E., 2000, MNRAS, 311, 629
Meurer G. R., Heckman T. M., Lehnert M. D., Leitherer C., Lowenthal J., 1997, AJ, 114, 54
Mo H. J., White S. D. M., 2002, MNRAS, 336, 112
Murray N., 2009, ApJ, 691, 946
Nesvadba N. P. H. et al., 2006, ApJ, 650, 661
Okamoto T., Eke V. R., Frenk C. S., Jenkins A., 2005, MNRAS, 363, 1299
Ouchi M., Shimasaku K., Okamura S., Furusawa H., Kashikawa N., Ota K., Doi M., Hamabe M., 2004, ApJ, 611, 685
Pettini M., Shapley A. E., Steidel C. C., Cuby J., Dickinson M., Moorwood A. F. M., Adelberger K. L., Giavalisco M., 2001, ApJ, 554, 981
Pettini M., Rix S. A., Steidel C. C., Adelberger K. L., Hunt M. P., Shapley A. E., 2002a, ApJ, 569, 742
Pettini M., Rix S. A., Steidel C. C., Hunt M. P., Shapley A. E., Adelberger K. L., 2002b, Ap&SS, 281, 461
Pryor C., Meylan G., 1993, in Djorgovski S. G., Meylan G., eds, ASP Conf. Ser. Vol. 50, Structure and Dynamics of Globular Clusters. Astron. Soc. Pac., San Francisco, p. 357
Richard J., Stark D. P., Ellis R. S., George M. R., Egami E., Kneib J.-P., Smith G. P., 2008, ApJ, 685, 705
Salpeter E. E., 1955, ApJ, 121, 161
Salucci P., Swinbank A. M., Lapi A., Yegorova I., Bower R. G., Smail I., Smith G. P., 2007, MNRAS, 382, 652
Shapley A. E., Steidel C. C., Pettini M., Adelberger K. L., 2003, ApJ, 588, 65
Soifer B. T., Neugebauer G., Franx M., Matthews K., Illingworth G. D., 1998, ApJ, 501, L171
Stark D. P., Swinbank A. M., Ellis R. S., Dye S., Smail I. R., Richard J., 2008, Nat, 455, 775
Stark D. P., Ellis R. S., Bunker A., Bundy K., Targett T., Benson A., Lacy M., 2009, ApJ, 697, 1493
Steidel C. C., Giavalisco M., Pettini M., Dickinson M., Adelberger K. L., 1996, ApJ, 462, L17
Swinbank A. M. et al., 2003, ApJ, 598, 162
Swinbank A. M., Bower R. G., Smith G. P., Smail I., Kneib J.-P., Ellis R. S., Stark D. P., Bunker A. J., 2006a, MNRAS, 368, 1631
Swinbank A. M., Chapman S. C., Smail I., Lindner C., Borys C., Blain A. W., Ivison R. J., Lewis G. F., 2006b, MNRAS, 371, 465
Swinbank A. M., Bower R. G., Smith G. P., Wilman R. J., Smail I., Ellis R. S., Morris S. L., Kneib J.-P., 2007, MNRAS, 376, 479

Tenorio-Tagle G., Silich S. A., Kunth D., Terlevich E., Terlevich R., 1999, MNRAS, 309, 332
Teplitz H. I. et al., 2000, ApJ, 533, L65
Vanzi L., Cresci G., Telles E., Melnick J., 2008, A&A, 486, 393
Verma A., Lehnert M. D., Förster Schreiber N. M., Bremer M. N., Douglas L., 2007, MNRAS, 377, 1024
White S. D. M., Rees M. J., 1978, MNRAS, 183, 341
Wilman R. J., Gerssen J., Bower R. G., Morris S. L., Bacon R., de Zeeuw P. T., Davies R. L., 2005, Nat, 436, 227
Wilson C. D., Matthews B. C., 1995, ApJ, 455, 125
Yoshida M. et al., 2006, ApJ, 653, 988

This paper has been typeset from a TEX/LATEX file prepared by the author.